



MIT Open Access Articles

Pulsed Heat Transfer for Thermal Maximum Power Point Tracking

The MIT Faculty has made this article openly available. **Please share** how this access benefits you. Your story matters.

Citation	McKay, Ian Salmon, and Evelyn N. Wang. "Pulsed Heat Transfer for Thermal Maximum Power Point Tracking." Proceedings of the ASME 2013 International Mechanical Engineering Congress and Exposition, 15-21 November, 2013, San Diego, California, USA, ASME, 2013. © 2013 by ASME
As Published	http://dx.doi.org/10.1115/IMECE2013-62998
Publisher	ASME International
Version	Final published version
Accessed	Fri Feb 01 20:23:10 EST 2019
Citable Link	http://hdl.handle.net/1721.1/120051
Terms of Use	Article is made available in accordance with the publisher's policy and may be subject to US copyright law. Please refer to the publisher's site for terms of use.
Detailed Terms	

IMECE2013-62998

Pulsed Heat Transfer for Thermal Maximum Power Point Tracking

Ian Salmon McKay

Department of Mechanical Engineering
Massachusetts Institute of Technology
Cambridge, MA, USA

Evelyn N. Wang

Department of Mechanical Engineering
Massachusetts Institute of Technology
Cambridge, MA, USA

ABSTRACT

This paper presents a new method for enhancing thermal energy harvesting via pulsed heat transfer. By acting as a variable thermal resistance that theoretically generates no entropy, a pulsed thermal connection allows calibration of the effective thermal resistance of an energy harvesting system. By adjusting the frequency and duty cycle of the pulsed heat transfer, the method allows an energy harvester to be continuously optimized for a variable incident heat flux. In this paper, the analysis of a generalized model shows how the pulse strategy theoretically allows any heat engine-heat sink pair to work at the same power and efficiency as a 1:1 thermal resistance-matched engine-heat sink pair of equal or greater total thermal resistance. Experiments with a mechanical thermal switch validate this model, and show how the pulse strategy can improve the efficiency of a system with equal engine and heat sink thermal resistances by over 80% with no increase in the hot-side maximum temperature, although at reduced total power. At a 1:2 engine-sink resistance ratio, the improvement can simultaneously exceed 60% in power and 15% in efficiency. The thermal pulse strategy could be implemented to improve a variety of systems that convert thermal energy, from waste heat harvesters to the radioisotope power systems on many spacecraft.

NOMENCLATURE

A Cross-sectional area (m^2)
 Bi Biot Number
 c Specific heat capacity (J/kgK)
 C^* Energy storage ratio $m_S c_S / m_R c_R$

D Duty cycle $t_o / (t_o + t_c)$
 Fo Lumped Fourier number $t / (Rmc)$
 L Characteristic length (m)
 m Mass (kg)
 P Output power (W)
 P^* Scaled power $PR / (T_\infty)$
 Q, q Input power (W)
 R Effective thermal resistance (K/W)
 R^* Thermal resistance ratio R_S / R_R
 T Temperature (K)
 T^* Scaled temperature $(T - T_{S,min}) / (T_{S,max} - T_{S,min})$
 t time (s)
 t^* Scaled time t / t_c
 α Fraction of Carnot efficiency
 δ Duty ratio t_o / t_c

Abbreviations:

OTS Oscillating Thermal Switch
PHF Pulsed Heat Flux
RPS Radioisotope Power System

Subscripts:

c Switch closed phase (heat flux on)
 E Heat engine
 o Switch open phase (heat flux off)
 R Heat rejection
 S Heat source
 SS Steady-state heat transfer
 ∞ Ambient condition

INTRODUCTION

Thermal energy is ubiquitous in nature, and thermal energy harvesters are a popular choice for many remote power applications [1, 2]. The performance of these systems, however, is often limited by the division of an overall steady-state temperature gradient between a heat engine and a heat sink, which confines the maximum figure of merit to scale with the engine-sink thermal resistance ratio [3, 4]. Since heat sink resistance is typically size-dependent, this limitation is often reflected as a tradeoff between efficiency and power density in energy harvester design [5]. This tradeoff in turn impacts the performance of a variety of crucial thermal systems, including waste heat energy harvesters, combustion-based harvesters used in remote areas, concentrated solar power (CSP) generators, and the radioisotope power systems (RPS) on many spacecraft [1, 5, 6, 7].

The challenge of high rejection-side temperature can be reduced in certain cases if the harvester receives thermal energy in distinct pulses, rather than operating at steady state. By taking advantage of the thermal impedances of the heat source and sink, pulsed heat transfer allows the maximum thermal gradients and heat fluxes in the system to be synchronized. The resulting phase lag between the system hot and cold side temperatures can allow a heat engine to work over a large thermal gradient, despite a conventionally unfavorable engine-sink thermal resistance ratio. This approach theoretically reduces the power and efficiency loss associated with the temperature drop across the heat sink in steady state operation. The thermal pulse mode may therefore enable the development of more effective energy harvesting systems and allow more flexibility in system design, especially for small-scale systems and those that process time-variant heat fluxes. Fig. 1 illustrates the effect of the thermal pulse mode schematically, and introduces two methods for inducing pulsed heat transfer.

An energy harvester can operate in a thermal pulse regime either by coupling to a pulsed heat flux (PHF), or by interfacing a constant heat source with an oscillating thermal switch (OTS). Examples of the PHF configuration of Fig. 1a include a periodically burning gas heater, intermittently flowing heat transfer fluid, or any other oscillating heat flux. Examples of the OTS configuration shown in Fig. 1b include any oscillating thermal connection between a constant heat source and a heat engine, *i.e.*, bistable thermal-fluid circuits such as the Tamburini T-system [8]. The coupling between the hot-side temperature and overall heat flux in the OTS configuration leads to behavior that is distinct from that of the PHF. By cycling between low and high thermal resistance states, the switch acts as variable thermal impedance that in theory generates no entropy. By varying the duty cycle of the switch, the thermal gradient can be adjusted to optimize the conversion efficiency of the heat engine, regardless of the engine thermal resistance or the source heat production.

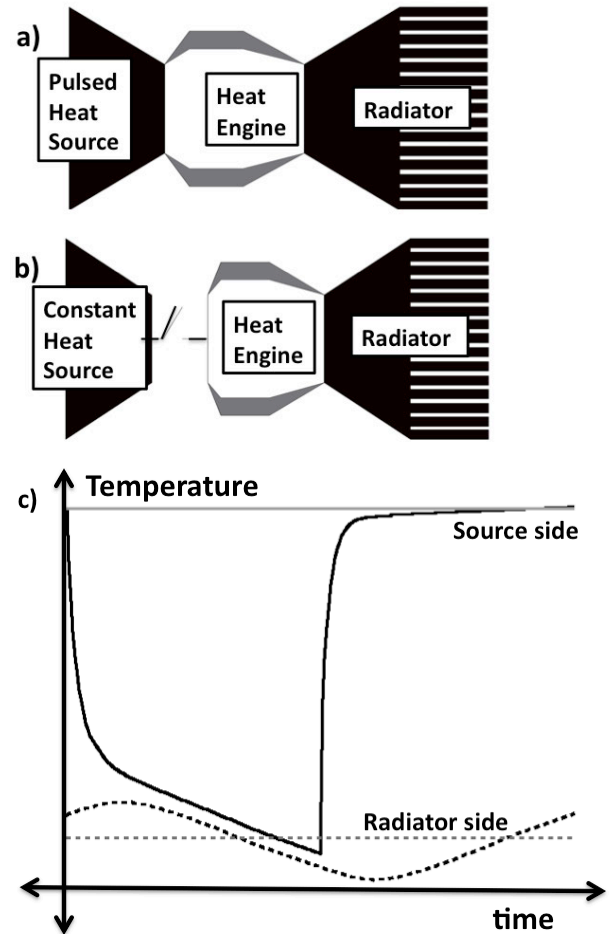


Figure 1. Generalized energy harvesters using a) a pulsed heat source and b) an oscillating thermal switch to achieve pulsed heat transfer. c) Schematic temperature traces showing heat engine hot side (solid) and cold side (dotted) temperatures with a pulsed heat source (black) and a steady one (gray) with the same time-averaged heat flux Q .

Thermal transient processes already drive a number of high-efficiency heat removal systems, including pulsating heat pipes [9], solid-state heat pumps [10], and phase change electronics cooling [11]. However, outside of work on pyroelectric and other solid-state phenomena [12, 13], little attention has been given to the potential benefit of the thermal pulse mode in an energy harvesting context. In this paper, we investigated both the PHF and OTS energy harvesting configurations. We developed a quasi-steady-state model of the pulsed heat flux system in Section 2. A similar model of the OTS (Fig. 1b) is developed in Section 3 and validated with proof-of-concept experiments in Section 4. The work shows potential opportunities in using thermal pulse energy conversion for increased efficiency and power output in applications ranging from remote power generation to waste heat recovery.

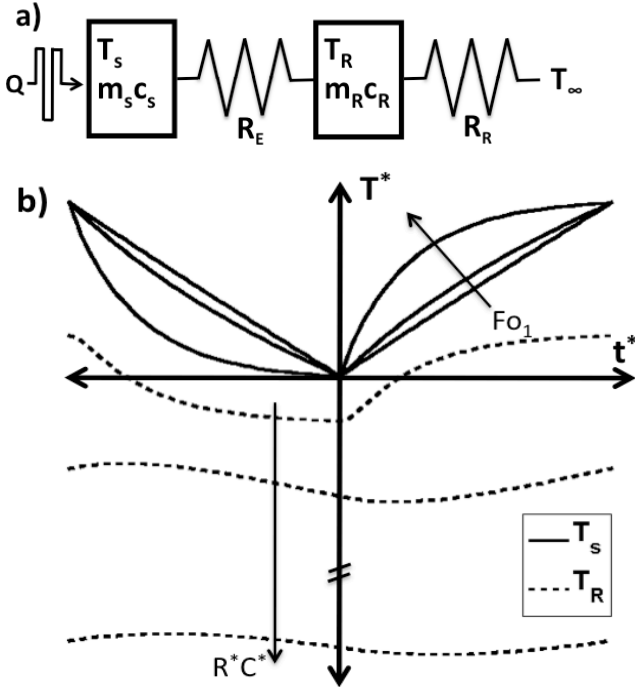


Figure 2. a) A lumped-parameter model for the PHF system depicted in Fig. 1a b) Non-dimensional temperature traces of the source and sink, where temperature $T^* = (T - T_{S,min}) / (T_{S,max} - T_{S,min})$ and time $t^* = t/t_c$ for temperature swing $(T_{S,max} - T_{S,min})$ and switch closed (heat flux on) time t_c .

2. A PULSED HEAT FLUX

We developed a generalized lumped model for the PHF configuration (Fig. 2a), consisting of a heat source, heat engine, and heat sink. We assume that there is negligible thermal energy storage inside the heat engine, that the internal impedances of the heat source and sink are small relative to that of the heat engine ($Bi \ll 1$), and that the heat production Q is a continuous square wave, with $Q=Q_o$ for time $0 < t < t_c$ and $Q = 0$ from $t_c < t < t_o$, where t_c is the duration of the thermal pulse and t_o the time between pulses. The temperature, mass, and specific heat of the heat source and sink are T_S and T_R , m_S and m_R , c_S and c_R , respectively. The thermal resistances of the heat engine and between the heat sink and ambient are R_E and R_R . Seven non-dimensional parameters describe the PHF system: the engine-sink thermal resistance ratio $R^* = R_E/R_R$, the source-sink energy storage ratio $C^* = m_S c_S / m_R c_R$, power production $Q^* = Q R_E / T_\infty$ and the bulk Fourier numbers $Fo_1 = t_c / (R_E m_S c_S)$ and $Fo_2 = t_o / (R_R m_R c_R)$, which are characteristic heating or cooling time scales for the source and heat sink, respectively. The heat engine efficiency η_E is also defined and assumed to scale by a constant factor α with the Carnot efficiency, $\eta_E = \alpha (1 - T_R/T_S)$.

The energy equations that describe the closed (heat flux on) and open (heat flux off) phases are:

$$\left. \frac{dT_S}{dt} \right|_{\text{closed}} = \frac{Q}{m_S c_S} - \frac{(T_S - T_R)}{R_E m_S c_S} \quad (1)$$

$$\left. \frac{dT_S}{dt} \right|_{\text{open}} = \frac{(T_S - T_R)}{R_E m_S c_S} \quad (2)$$

$$\left. \frac{dT_R}{dt} \right|_{\text{open/closed}} = (1 - \eta_E) \frac{(T_S - T_R)}{R_E m_R c_R} - \frac{(T_R - T_\infty)}{R_R m_R c_R} \quad (3)$$

Equations 1 and 2 represent the rate of change of the heat source temperature T_S in the switch-closed and switch-open phases, respectively. Equation 3 expresses the rate of change of the heat sink temperature T_R . This formulation is based on the lumped-parameter model in Fig. 2a, with the heat engine modeled as a thermal resistance R_E that extracts a fraction η_E of the thermal energy that flows through it. The equations are solved recursively, with the initial condition for the closed phase equal to the final condition for the open phase and vice versa. Fig. 3a shows the theoretical efficiency of a PHF system normalized to that of a steady-state harvester operating with the same $T_{max}/T_\infty = 1.5$ and $R^* = 0.1$, for a variety of the characteristic time scales Fo_1 and Fo_2 . Here $R^* = C^* = 0.1$ and $\alpha = 1$. Fig. 3b shows the theoretical output power P of the PHF model for the same conditions. In each of these simulations, the heat flux Q was set so that the maximum temperature $T_{max} = 1.5 T_\infty$, so that the analysis applied to real systems with finite maximum hot-side temperatures.

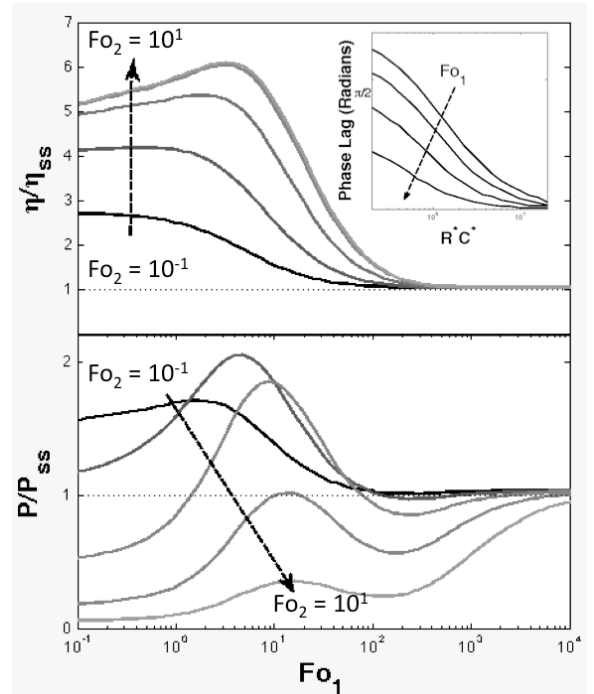


Figure 3. (top) Efficiency η and (bottom) output power P of PHF energy conversion with Fo_1 and Fo_2 , normalized to the steady-state performance P_{SS} and η_{SS} under the same conditions.

The model indicates that increasing Fo_2 always improves energy conversion efficiency by ensuring that the heat sink has cooled towards T_∞ at the start of each energy conversion cycle. For improved output power, however, the trend is reversed; shorter Fo_2 is preferred, and the maximum power occurs at larger Fo_1 . This trend is due to slower warming of the heat sink upon each switch-closed phase with increasing Fo_2 . The inset of Fig. 3a shows that the phase lag, defined as the delay in radians between the minimum values of T_s and T_R , are maximized at low Fo_1 . However, in this region both power and efficiency are low as a result of lower time-averaged T_s attributed to the longer switch-closed phase. Therefore, the optimum for both power and efficiency is at an intermediate Fo_1 , where T_s is close to T_{max} for most of the energy conversion phase, and the phase lag is relatively small.

Fig. 4 compares the efficiency and non-dimensional power $P^* = P(R_S + R_R)/T_\infty$ of the PHF and steady-state strategies at the same maximum temperature difference T_{max}/T_∞ for a variety of R^* and C^* . In this figure, $Fo_1 = 5$ and $Fo_2 = 1$, these are near the optimal values for low R^*C^* suggested in Fig. 3. Clearly, suitable values of these time scales can allow the PHF exceed the steady state efficiency for almost any system configuration, with over a 50% advantage over steady state η at $R^* = 1$. However, the PHF can only achieve higher power than steady state for systems with low R^*C^* . Both output power and efficiency increase with increasing R^* , with larger increases predicted for efficiency than for power. Additionally, the steady-state performance shows more variability with changing R^* than the thermal pulse mode, reflecting the effective boost in R^* given by the higher effective resistance R_E at duty cycle $D < 1$. The power and efficiency boost by $R^* = 0.1$ can exceed 150%, as shown in Fig. 3.

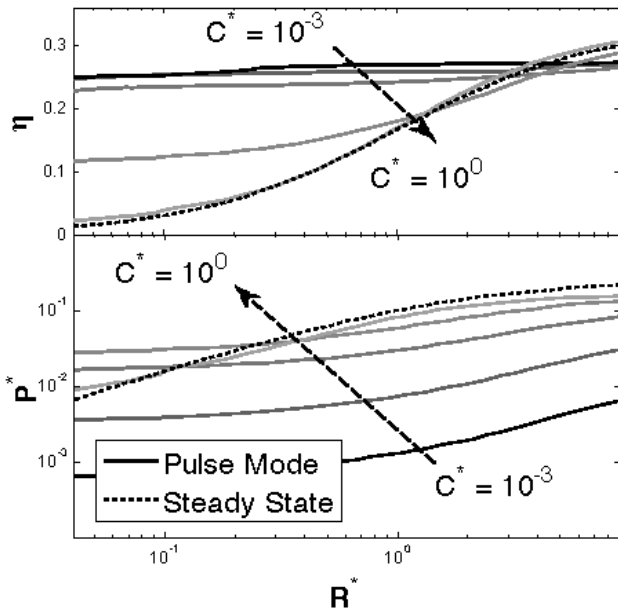


Figure 4. Comparison of the power and efficiency of the pulse and steady-state energy conversion regimes for fixed temperature bounds.

2.1 Pulsed Temperature Input

An important special case of the PHF model occurs when $Fo_1 \ll 1$, $C^* \ll 1$ and the heat flux Q is delivered as sharply declining pulse, as shown in Fig. 5. This case corresponds to a square-wave input on the hot side temperature T_s . With T_s specified, the governing equations can be written for T_R alone:

$$\left. \frac{dT_R}{dt} \right|_{\text{closed}} = (1 - \langle \eta_E \rangle) \frac{(T_{max} - T_R)}{R_E m_R c_R} - \frac{(T_R - T_\infty)}{R_R m_R c_R}$$

$$\left(\langle \eta_E \rangle = \frac{\int_0^{t_c} \alpha(1 - T_R/T_{max}) dt}{t_c} \right) \quad (4)$$

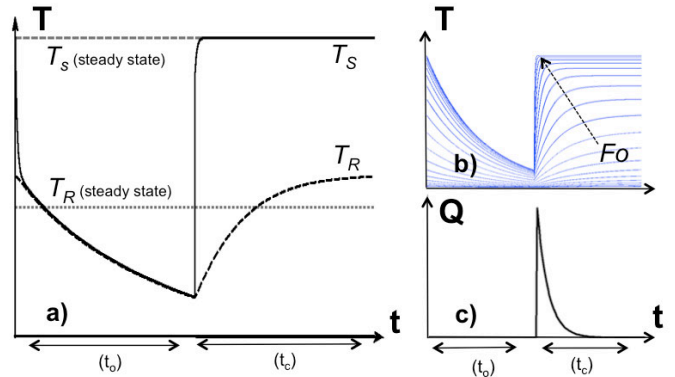


Figure 5. Schematics of a) temperature T_R , b) the variation of T_R with Fo , and c) thermal input power. All traces are for the special case of small Fo_1 and C^* analyzed in this section.

The boundary conditions are the same as (3). Linearizing the heat engine efficiency $\eta_E = \alpha(1 - T_R/T_s)$ over the period t_c yields an analytical expression for T_R :

$$T_R(t) = \frac{R_E T_\infty + R_R T_{max}(1 - \langle \eta_E \rangle)}{R_E + R_R(1 - \langle \eta_E \rangle)} + K e^{-t \frac{(R_E + R_R(1 - \langle \eta_E \rangle))}{m_R c_R R_R R_E}}$$

$$K = \frac{\left(-\frac{t_c}{e^{m_R c_R R_R}} \left(\frac{t_0}{e^{m_R c_R R_R}} - 1 \right) R_R (T_\infty - T_{max})(1 - \langle \eta_E \rangle) \right)}{\left(\frac{t_c + t_0}{e^{m_R c_R R_R}} - e^{-\frac{t_c(1 - \langle \eta_E \rangle)}{m_R c_R R_E}} \right) (R_R + R_R(1 - \langle \eta_E \rangle))} \quad (5)$$

A characteristic timescale of this system is $Fo = t_c/(R_E m_R c_R)$. As shown in Fig. 6, the pulse temperature input results in similar relationships between the timescales δ and Fo and the performance η and P as the pulse heat flux model. However, Figures 6c and 6d clearly show how the square wave temperature input offers better performance than the square wave heat flux input. For optimized δ and Fo , the pulse mode can equal the maximum-power ($R^* = 1$) performance of the steady state mode for any R^* , and can surpass the steady-state performance in both power and efficiency for all $R^* < 1$. This

represents an enhancement of approximately 65% in efficiency and 20% in power by $R^* = 0.5$, and nearly a four-fold boost in both power and efficiency by $R^* = 0.1$. As shown in Figures 6a and 6b, the point of inflection for $P/P_{SS, Max}$ and $\eta/\eta_{SS, Max}$ both occur at increasing Fo with increasing δ . At $R^* = 1$, the thermal pulse and steady state performance are identical for suitable values of the timescales δ and Fo .

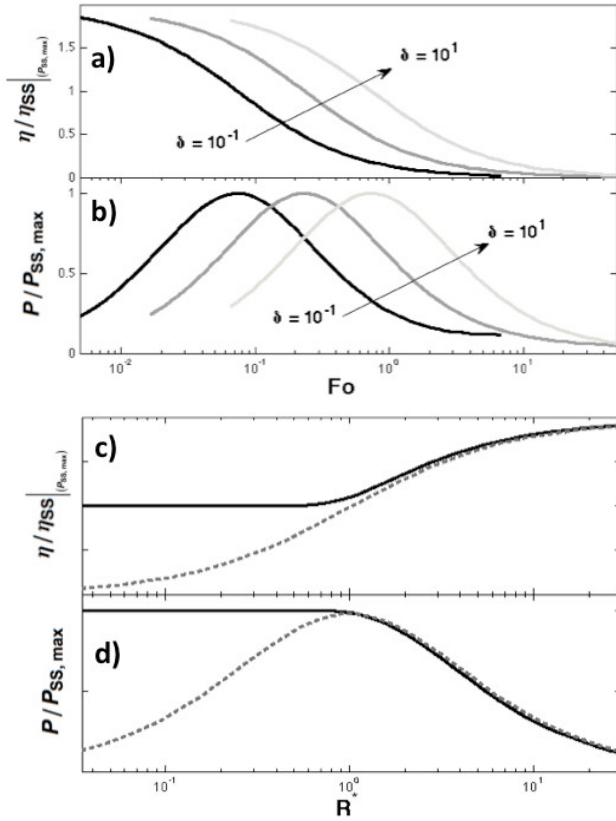


Figure 6. The variation in a) power and b) efficiency of the pulsed mode with the actuation timescale Fo , normalized to the maximum power ($R^* = 1$) steady state performance. At suitable Fo , the pulse mode can match or beat the steady state mode in either power or efficiency, but cannot exceed it in both simultaneously. The power and efficiency of both modes are shown relative R^* in c) and d).

3. AN OSCILLATING THERMAL SWITCH

A second approach to pulsed thermal energy conversion is to position an oscillating thermal switch between a constant heat source and a heat engine, as shown schematically in Fig. 7a. The strategy applies to systems with a contained heat source and thermal energy storage capacity, so that energy is not lost to the surroundings during the switch-open phase. The assumptions underlying the OTS model are the same as for the PHF, with the exception of a constant heat source Q and a lossless and discrete thermal switch between the source and engine.

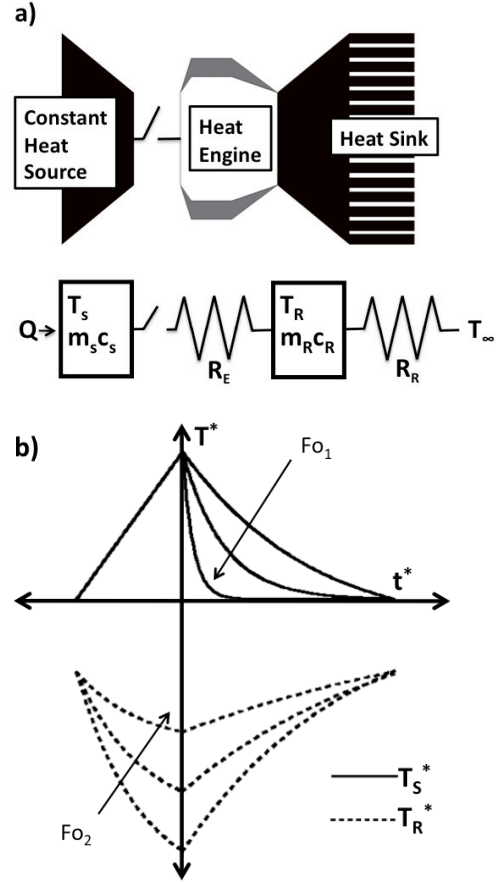


Figure 7. a) OTS system (top) reduced to a lumped-parameter model (bottom). b) Non-dimensional temperature traces of the source and sink for different values of the characteristic time scales Fo_1 and Fo_2 .

T_S and T_R for the quasi-steady state OTS system can be described both dimensionally and in terms of the scaled temperature $T^* = (T - T_{S,min}) / (T_{S,max} - T_{S,min})$ and time $t^* = t/t_c$:

$$\left. \frac{dT_S}{dt} \right|_{\text{closed}} = \frac{Q}{m_s c_s} - \frac{(T_S - T_R)}{R_E m_s c_s}$$

$$\left. \frac{dT_S^*}{dt^*} \right|_{\text{closed}} = \frac{Fo_1}{Fo_2} R^* C^* - Fo_1 (T_S^* - T_R^*) \quad (6)$$

$$\left. \frac{dT_R}{dt} \right|_{\text{closed}} = (1 - \eta_E) \frac{(T_S - T_R)}{R_E m_R c_R} - \frac{(T_R - T_\infty)}{R_R m_R c_R}$$

$$\left. \frac{dT_R^*}{dt^*} \right|_{\text{closed}} = Fo_1 C^* [(1 - \eta_E) (T_S^* - T_R^*) - R^* (T_R^* - T_\infty^*)] \quad (7)$$

Fig. 7b shows schematic traces for T_S^* and T_R^* for different Fo_1 and Fo_2 . The first term in (4) is equivalent to the duty ratio $\delta = t_i/t_o$, while in both (4) and (5) the coefficients of the

temperature terms are the time constants of the switch-closed phase. The boundary conditions are given by the equations for the switch-open phase, when the heat source warms in isolation and the heat sink cools towards T_∞ .

$$\left. \frac{dT_S^*}{dt^*} \right|_{\text{open}} = \delta \quad \rightarrow T_S^*(0) = 1 \quad (8)$$

$$\left. \frac{dT_R^*}{dt^*} \right|_{\text{open}} = -Fo_2(T_R^* - T_\infty^*) \\ \rightarrow T_R^*(0) = T_\infty^* + (T_R^*(-1/\delta) - T_\infty^*) e^{-Fo_2} \quad (9)$$

Fig. 8 shows the normalized efficiency and temperature for $C^*=R^*=Q^*=\alpha = 1$. Fig. 8a shows that in the absence of a maximum operating temperature, a lower switch duty ratio δ always leads to a higher temperature ratio T_S/T_R , and therefore to more-efficient energy conversion. Fig. 8b shows how the minimization of the characteristic time Fo_1 and the maximization of Fo_2 increases the theoretical energy conversion efficiency regardless of the maximum temperature reached.

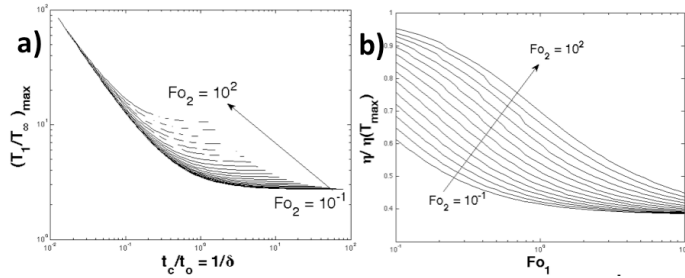


Figure 8. a) Maximum normalized operating temperature as a function of the duty ratio $\delta = t_o/t_c$ and Fo_2 . b) Efficiency of the OTS model in terms of the non-dimensional time scales Fo_1 and Fo_2 .

The limit of $Fo_1 \ll 1$ and $\delta, Fo_2 \gg 1$ corresponds to an operating condition in which the heat sink cools to T_∞ on every switch-open phase and the source temperature remains nearly constant during each switch-closed phase. The maximum efficiency of the OTS model is expected at the maximum possible value of Fo_2 and the minimum value of Fo_1 , where δ is set to keep $T_{S,\text{max}}$ as close as possible to the temperature tolerance of the system.

3.1 A SPECIAL CASE: CONSTANT HEAT SINK TEMPERATURE

Since many energy harvesters are attached to vehicles or other sinks of comparatively large thermal mass, a case where $C^* \approx 0$ and the heat sink temperature is practically constant may be realistic. The $C^* \approx 0$ condition could also reflect the thermal arrest that would result from incorporating a phase change material heat sink. In this case, $T_R = T_\infty + R_R Q$, and the characteristic time scale of the system reduces to Fo_1 alone.

This model has a closed-form solution for the energy-conversion temperature gradient T_S/T_R :

$$\frac{T_S}{T_R} = 1 + \frac{Q}{T_R} \left(R_E + \frac{t_o}{m_s c_s} \frac{e^{\frac{t_c - t}{R_E m_s c_s}}}{e^{\frac{t_c}{R_E m_s c_s}} - 1} \right) \quad (10)$$

For the maximum efficiency case of $\delta \gg 1, Fo_1 \ll 1$, the temperature simplifies to $T_S/T_\infty = 1 + Q^*(\delta + 1)$, and the conversion efficiency is given by $\alpha Q^*/(D + Q^*)$ for duty cycle $D = 1/(\delta + 1)$. Because both the source and sink temperatures are effectively constant during the switch-closed phase with $Fo_1 \ll 1$, the temperature gradient reflects the effective thermal resistance of a rapidly switched connection with resistance R_{sw} between two infinite thermal reservoirs: $R_{\text{Eff}} = R_{sw}/D$. For a $C^* \approx 0$ system operating in these conditions, the maximum temperature T_{max} corresponds to the duty cycle $D = Q^*/(T_{\text{max}}/T_\infty - 1)$.

4. EXPERIMENTAL VALIDATION

We conducted proof-of-concept experiments to both validate the models of section 3 and investigate the potential of the OTS strategy. In one set of experiments, a $C^* = 0$ test apparatus was used to validate equation (8) and the maximum efficiency case over a range of Fo . In a second set of experiments, we compared an OTS system at favorable Fo_1 and Fo_2 to an equivalent steady-state system for a variety of R^* and C^* , while limiting both systems to the same maximum temperature.

As shown in Fig. 9a, an externally-powered bistable latching solenoid (Shenzhen Appliances ZHO-1253) driven by a PIC24 controller was used to physically move a heated block into and out of contact with either a thermoelectric generator (Marlowe TG-12) connected to a large copper heat sink for the $C^* = 0$ case described in Section 4.1, or with a simulated heat engine-heat sink combination (for the general case described in Section 4.2). The heat source consisted of a 4 cm x 4 cm copper block with an enclosed 10W 3 cm x 3 cm Kapton heater (Omega KHLV-101), and was connected to the solenoid actuator via 1.5 cm of steel wire-bonded carbon aerogel to prevent transfer to or from the actuator. The thermal leak rate of this configuration was measured at < 200 mW at a temperature difference of 20°C with the solenoid in the open position (as shown in Fig. 9a). A compliant graphite-polymer interface (Panasonic PGS) was used to ensure identical contact resistance for both the steady-state and OTS tests. The tests were conducted in a vacuum chamber at a pressure under 500 Pa to minimize convective heat loss. The microcontroller was used to set the duty cycle D and latching period, the heater was activated, and the system was allowed to oscillate until a stable oscillation had been reached before measurement commenced. In both cases, the temperatures T_S and T_R were measured using J-type thermocouples and used to infer the energy conversion potential of the simulated heat engine; the thermoelectric generator was left in an open-circuit condition to ensure nearly temperature-independent thermal resistance, preserving the generality of the results. T_∞ in these experiments was measured at the heat sink

base as 19°C. Data from the temperature measurements were collected using a computer-connected thermocouple data acquisition unit (National Instruments Ni eDAQ-9174). In all experiments, Q ranged from 1-40W and D ranged from 0.02 to 0.9, with an overall actuation period between 3s and 80s.

4.1 CONSTANT HEAT SINK TEMPERATURE

For the constant heat sink temperature case, the duty cycle of the connection was calibrated to keep the maximum temperature of the heat source constant at $T_{\max}/T_{\infty} = 1.25$ during steady oscillation. This experiment confirmed the interdependence of Fo_1 and η , for the case where $\alpha = 1$, $C^* = 0$ and $Q^* = .01$ from the model. The theoretical maximum efficiency was calculated from the average of η_{Carnot} over the heat flux. Fig. 9b shows the experimental results compared with both the exact solution and the approximation $\eta = \alpha Q^*/(D+Q^*)$. As shown, the exact solution is in good agreement with the actual performance, and converges towards the approximate solution at very low Fo_1 as expected. The small discrepancy is likely due to a combination of imperfect thermal isolation of the simulated heat source, parasitic contact resistance on the hot-side compliant thermal interface, finite thermal gradients inside the heat sink, and unaccounted-for effects of the thermal energy storage in the simulated heat engine, which would bring the solution closer to the $D = 1$ behavior. The error bars are associated with the standard deviation in calculated η between successive energy conversion periods, and may be associated with irregular contact resistance upon the switch closing. Because the duty cycle D was small in these experiments, the OTS efficiency stays well above the steady-state efficiency with identical Q^* , which resulted in a far lower hot-side temperature.

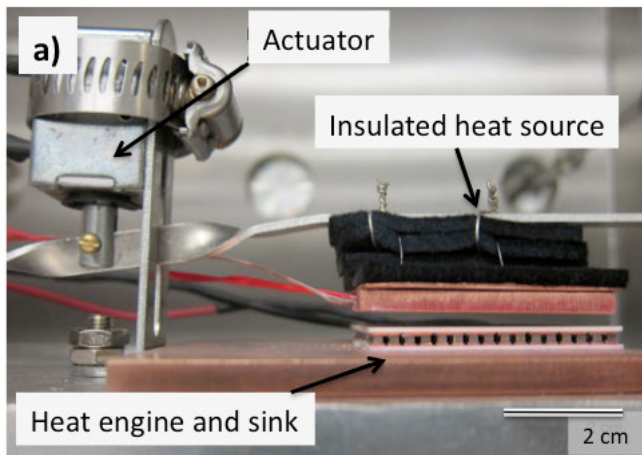


Figure 9 a) Proof-of-concept thermal switch experiment in a vacuum chamber.

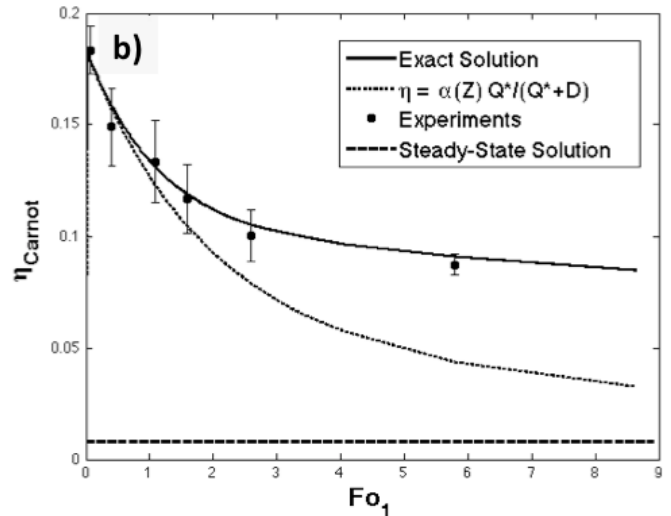


Figure 9 b) Average theoretical energy conversion efficiency η_{Carnot} based on experimental temperature measurements for the oscillating switch system ($\alpha = 1$, $C^* = 0$, $Q^* = .01$). The steady-state trace shows the performance of the same system at $Q^* = .01$.

4.2 A GENERAL OSCILLATING THERMAL SWITCH

This test evaluated the OTS strategy for a system with a real heat sink, $C^* \neq 0$, for a variety of R^* . We modified the experimental setup of Fig. 9a to include two thermal resistors (4 cm x 4 cm, 0.5mm thick insulating polyurethane gasket material) and a 7 mm thick 4 cm x 4 cm copper block in place of the thermoelectric generator, emulating the engine resistance R_E , heat sink resistance R_R , and heat sink thermal mass $m_s c_s$, respectively. All other components were left unchanged from the configuration shown in Fig. 9a. This apparatus can be seen in both the switch-open and switch-closed positions in the thermal images of Fig. 10. In order to test different values of R^* , gasket material was layered to form overall thermal resistances of various thicknesses between the blocks. R^* was then measured based on the steady-state temperature differences between the blocks T_S , T_R , and T_{∞} at steady state when a heat flux of 5 W was applied with the thermal switch in the closed position. These inert thermal resistors are highlighted in Fig. 10a for a configuration with $R^* = 1$. The test apparatus was painted black to enable quantitative temperature measurement with an infrared camera (Fluke SC6000, measured temperatures were verified with a J-type thermocouple) The actuation time scales were set to the near-optimal $Fo_1 = 0.1$ and $Fo_2 = 10$, and the heat flux Q set such that the maximum temperature ratio T_{\max}/T_{∞} did not exceed 1.5 at any point in the actuation cycle. Monitoring both T_S and T_R , we were then able to compare the steady-state and OTS performance for a variety of R^* and C^* . Fig. 10 highlights the higher average energy conversion temperature gradient of the OTS strategy relative to the steady-state strategy. Fig. 11 shows the variation in η with R^* in this test, highlighting the ability of the OTS system to maintain near-optimal efficiency for a range of system configurations.

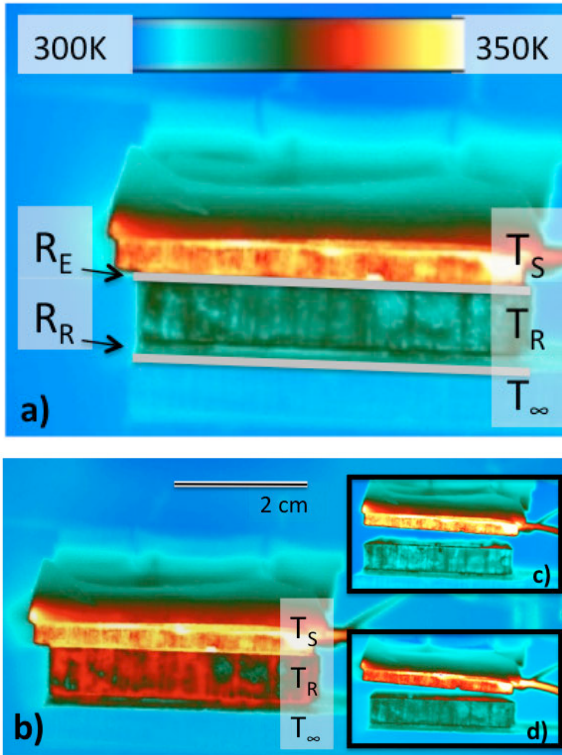


Figure 10. Infrared image of the test system, showing the two inert thermal resistors placed between the source, heat sink, and ambient blocks. a) The thermal gradient during the middle of the switch-closed phase of the OTS cycle thermal gradient for $C^* = 0.5$, $R^* = 1$ and $T_{max}/T_{\infty} = 1.5$. b) The steady-state temperature profile for the same conditions. The inset shows the OTS system an instant before (c) and an instant after (d) the switch-closed period.

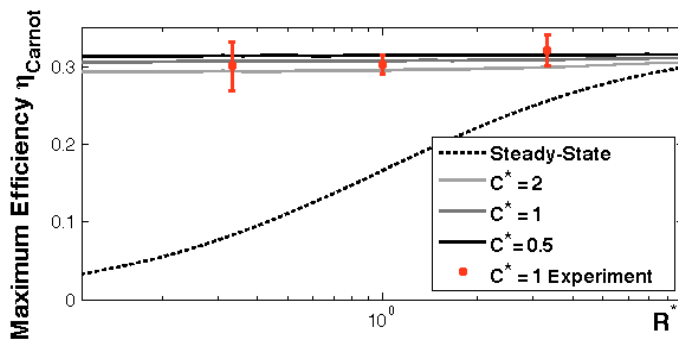


Figure 11. Performance comparison between the OTS and steady-state energy harvesting strategies for a variety of C^* and R^* , all held to $T_{max}/T_{\infty} = 1.5$ and working at quasi-optimal $Fo_1 = 0.1$, $Fo_2 = 10$. The experimental results are for the $C^* = 1$ system shown in Fig. 10.

Fig. 11 confirms that the OTS strategy has considerable efficiency advantages over steady-state heat flow over a range of R^* . For all values of R^* , the OTS system was able to maintain a temperature difference over the heat engine comparable to that observed in the case of $R^* \gg 1$ at steady state operation. However, these advantages should be understood in context of the lower power of the OTS system. Due to the higher effective thermal resistance of the OTS connection, an OTS system with a given maximum hot-side temperature must process a lower time-averaged heat flux than an identical system without a thermal switch. For the PHF model, this effect can be overcome by running the system at lower R^* and delivering heat in short bursts, enabling high power operation. In contrast, the maximum heat flux over the engine in the OTS model is coupled to the heat source temperature T_S . As a result, given a maximum hot-side temperature, the OTS can improve energy conversion efficiency over an optimized steady-state strategy, but at the expense of lower specific power.

5. DISCUSSION

In this paper, we developed two models of thermal pulse energy conversion, one based on a periodic heat flux (PHF), and another based on a periodic connection to a constant heat source (OTS). Additionally, two important sub-cases were investigated, representing thermal switching to constant hot- and cold-side temperatures, respectively. For a fixed system resistance $R_R + R_E$ and temperature bounds T_{max} and T_{∞} , the OTS strategy is ideally suited to increase the energy conversion efficiency at low power across a range of R^* , and its high and variable thermal impedance could also help small systems maintain a higher hot-side temperature than is typically possible. In contrast, the PHF strategy is capable of increasing both efficiency and power, though the combination of the two cannot exceed the steady-state maximum for optimized R^* . While the behavior of the PHF and OTS systems differ, in both cases the energy conversion enhancement is attributable to effective adjustment in R_E with changing D .

Of the thermal pulse models examined in this paper, the best performance is predicted for a system subjected to a pulsed hot-side temperature input (Section 2.1). This strategy theoretically allows an energy harvester to work at the system maximum power point (usually attainable only at $R^* = 1$) at any R^* [5]. Similar to the OTS, it also enables the system to approach the maximum possible efficiency $\eta_E = \alpha(1 - T_{\infty}/T_{max})$ at any R^* , although at a lower power.

The parameter R^* has a critical influence on the applicability of the thermal pulse strategy to real thermal energy harvesting systems. Energy harvester efficiency naturally increases with R^* , as a greater fraction of the available thermal gradient is concentrated over the heat engine at high R^* . However, this effect is balanced by a drop in system power with increasing total thermal resistance $R_E + R_R$ for a prescribed temperature difference $T_{max} - T_{\infty}$. As a

result, systems are typically designed for $R^* \geq 1$, while the total thermal resistance $R_E + R_R$ is calibrated to keep the heat source at its maximum stable temperature [5]. By allowing adjustment in the effective R_E by changing D , the thermal pulse strategy therefore can outperform the traditional steady state strategy in two distinct cases: when external considerations prohibit the design of an energy harvester with optimal R^* , or when a change in operating conditions changes the optimal total thermal resistance $R_E + R_R$ required to maintain the heat source at its maximum temperature.

Design constraints, however, can restrict the range of attainable R^* in a thermal energy harvester. Lower than optimal R^* is most likely to occur in small-scale systems; R_R typically increases with decreasing system size, as the heat rejection area decreases, while R_E tends to decrease with decreasing size, as the conduction or mass transfer path length increases. For example, if the energy harvester of Fig. 1a) uses a thermoelectric generator and a convective heat sink, R_E increases in proportion to the characteristic length L , while R_R decreases with L^2 [14]. Suboptimal R^* could also result from cost considerations; for example, the choice of a thin-film thermoelectric heat engine of low R_E could lower device cost, but at the expense of R^* . By implementing a thermal pulse strategy, this choice could be made without sacrificing output power or efficiency.

Variable operating conditions can also affect the optimal total system resistance $R_E + R_R$. For a system constrained by a certain T_{max} , a change in incident heat flux Q or ambient temperature T_∞ could lead to either reduced output power or damage to the energy harvester. Because of the change in effective R_E with D , the thermal pulse mode therefore allows a system to maintain optimal $R_E + R_R$ across a range of operating conditions. For such systems, an adjustment in D to match the incident flux would constitute a new type of thermal maximum power point tracking.

While these advantages may make the thermal pulse mode naturally suited to small-scale energy harvesters and those that operate in variable conditions, the application to more traditional systems is also of interest. Fig. 12 shows generalized schematics of two such systems. The gas-fired chiller in Fig. 12a) represents a direct application of the PHF model of Section 2. Fig. 12b) depicts a general energy converter, such as a solar-thermal power plant using a PHF strategy. By cycling heat transfer fluid between two engine-heat sink pairs, the system could benefit from the efficiency boost of the PHF without the power loss even at higher R^* . By incorporating thermal energy storage in the form of high C_s , this system could deal with spikes in energy demand simply by changing the duty cycle D , effectively applying the PHF strategy to the problem of grid-scale energy storage. In a variant of Fig. 12b), the PHF might also be implemented with a naturally oscillatory conversion process, such as in pyroelectric or thermochemical converters [11, 15].

Promising future work might include an analysis of the thermal pulse mode in the context of one of these oscillatory conversion processes.

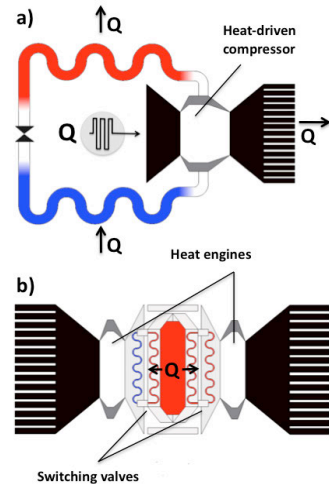


Figure 12. a) Example application of thermal pulse energy conversion in a gas-fired chiller. b) The thermal pulse strategy in an energy harvester that uses a constant heat source, such as an RPS.

6. CONCLUSIONS

This paper presents a new means of enhancing thermal energy conversion with pulsed heat transfer. In most cases, transient-regime operation can allow an energy harvester to more effectively divide an available temperature difference between its heat engine and heat sink. If controlled properly, this effect can be exploited to increase the efficiency and power density of systems that operate at a non-optimal engine-heat sink resistance ratio R^* . Furthermore, by changing the pulse duty cycle, the energy harvester can maintain optimal power and efficiency even as incident heat flux Q and ambient temperature T_∞ vary. The enhancement increases at lower R^* , where traditional conversion strategies break down. The theoretical efficiency improvement for a system with $R^* = 1$ could exceed 80% with reduced output power, while the improvement for an $R^* = 0.5$ system could exceed 60% in power and 15% efficiency, without any increase in the system hot-side temperature. The maximum efficiency of the pulsed heat flux model occurs at the maximum possible value of the time scale Fo_2 , low Fo_1 , and the duty cycle D that keeps T_5 as near as possible to the maximum temperature. The maximum power is also reached at low Fo_1 , but at more intermediate Fo_2 and higher D . The high and variable thermal impedance of the periodic thermal connection may be particularly useful for systems that work at small scales or with time-varying thermal energy loads, and could help allow for far more flexibility in energy harvester design. Future work may include an expanded treatment of the governing equations tailored towards a specific type of thermal energy harvester, or an analysis of suitable methods of inducing pulsed heat transfer from a constant heat source.

ACKNOWLEDGMENTS

The authors graciously acknowledge assistance from Nenad Miljkovic, Andrej Lenert and Dan Kraemer of M.I.T.

REFERENCES

- [1] Gur I, Sawyer K, Prasher R. Searching for a better thermal battery. *Science* 2012 335(1).
- [2] Hall, W. Terrestrial applications of thermoelectric generators. *Handbook of thermoelectrics* CRC Press 1995; 503
- [3] Sonntag R, Borgnakke C, Wylen G. *Fundamentals of thermodynamics* 6th ed. John Wiley and Sons 2003; 232
- [4] Bierschenk J. Optimized thermoelectrics for energy harvesting applications. *Energy harvesting technologies*. Springer 2009; 337-349
- [5] Snyder G. Thermoelectric energy harvesting. *Energy harvesting technologies*. Springer 2009; 325-336
- [6] Mason L. Realistic specific power expectations for advanced radioisotope power systems. *Journal of propulsion and power* 2007; 23(5): 1075-1079
- [7] Wagner M, Kutscher C. Assessing the impact of heat rejection technology on CSP plant revenue. *SolarPACES* 2010
- [8] Weislogel M. Passive oscillatory heat transport systems. *AIP Conf. Proc.* 2002; 608: 241-248
- [9] Akachi H. Structure of a heat pipe, US Pat. No. 4,921,041, 1991
- [10] Snyder G, Fleurial J, Caillat T, Yang R, Chen G. Supercooling of peltier cooler using a current pulse. *Journal of applied physics* 2002; 92[3]: 1564-9
- [11] Kandasamy R, Wang X, Mujumdar A. Transient cooling of electronics using phase change material (PCM)-based heat sinks. *Applied thermal engineering* 2008, 28(8-9)
- [12] Hunter N, Lavrick N, Bannuru T, Mostafa A, Rajic S, Datskos P. Development of MEMS-based pyroelectric thermal energy harvesters. *Proc. of SPIE* 2011; 8035: 80350V
- [13] Choi W, Hong S, Abrahamson J, Han J, Changsik C, Nair N, Baik S, Strano M. Chemically driven carbon-nanotube-guided thermopower waves. *Nature Materials* 2010; 9(5): 423-9
- [14] Incropera F, Dewitt D, Bergman L, Lavine A. *Introduction to heat transfer*, 5th ed, John Wiley & Sons, 2007;485
- [15] Vining C, Williams R, Underwood M, Ryan M, Suitor J. Reversible thermodynamic cycle for AMTEC power conversion. *J. Electrochem. Soc.* 1993; 140(10):2760-2763.